ELSEVIER

Kinetic measurement and prediction of the hydrogen outgassing from the polycrystalline LiH/Li₂O/LiOH system

L.N. Dinh [a,*], D.M. Grant [b], M.A. Schildbach [a], R.A. Smith [c], W.J. Siekhaus [a], B. Balazs [a], J.H. Leckey [c], J.R. Kirkpatrick [d], W. McLean II [a]

[a] *Lawrence Livermore National Laboratory, Chemistry and Materials Science, P.O. Box 808, L-092, Livermore, CA 94552, USA*
[b] *Atomic Weapons Establishment, Aldermaston, UK*
[c] *BWXT Y-12, Oak Ridge, TN, USA*
[d] *Oak Ridge National Laboratory, Oak Ridge, TN, USA*

Abstract

Due to the exothermic reaction of lithium hydride (LiH) salt with water during transportation and handling, there is always a thin film of lithium hydroxide (LiOH) present on the LiH surface. In dry or vacuum storage, this thin LiOH film slowly decomposes. The technique of temperature-programmed reaction/decomposition (TPR) was employed in combination with the isoconversion method of thermal analysis to determine the outgassing kinetics of H_2O from pure LiOH and H_2 and H_2O from this thin LiOH film. H_2 production via the reaction of LiH with LiOH, forming a lithium oxide (Li_2O) interlayer, is thermodynamically favored, with the rate of further reaction limited by diffusion through the Li_2O and the stability of the decomposing LiOH. Lithium hydroxide at the LiOH/vacuum interface also decomposes easily to Li_2O, releasing H_2O which subsequently reacts with LiH in a closed system to form H_2. At the onset of dry decomposition, where H_2 is the predominant product, the activation energy for outgassing from a thin LiOH film is lower than that for bulk LiOH. However, as the reactions at the LiH/Li₂O/LiOH and at the LiOH/vacuum interfaces proceed, the overall activation energy barrier for the outgassing approaches that of bulk LiOH decomposition. The kinetics developed here predict a hydrogen evolution profile in good agreement with hydrogen release observed during long term isothermal storage.
© 2005 Elsevier B.V. All rights reserved.

1. Introduction

Lithium hydride (LiH) salt has a high affinity for water. The reaction of hydride with water generates hydrogen gas and heat, the effects of which may be undesirable and pose compatibility or safety issues under certain circumstances. Many different aspects of the reaction of H_2O with LiH to form hydrogen have been investigated in careful detail [1,2]. Even in the absence of a H_2O releasing source, hydrogen generation from within the LiH/Li₂O/LiOH surface layers has been reported [3–5]. There have also been efforts to qualitatively explain and to partially approximate hydrogen outgassing based on the

* Corresponding author. Tel.: +1 925 422 4271; fax: +1 925 424 4737.
  E-mail address: dinh1@llnl.gov (L.N. Dinh).

experimental existence of some form of unstable LiOH [4,5]. However, there is no public record of a complete and quantitative study of the hydrogen outgassing profile from the $LiH/Li_2O/LiOH$ system.

This report presents the use of temperature programmed reaction/decomposition (TPR) in the isoconversion mode, in conjunction with field emission scanning electron microscopy (SEM) and atomic force microscopy (AFM) to (1) identify possible hydrogen producing reaction pathways, (2) measure the outgassing kinetics and (3) make kinetic predictions concerning hydrogen outgassing from the polycrystalline $LiH/Li_2O/LiOH$ system in the absence of any external H_2O source.

2. Experiments

The surface roughness of a typical pressed polycrystalline salt sample was probed with a commercial AFM (Digital Nanoscope IV in tapping mode) in ambient air. A Hitachi field emission scanning electron microscope (model S4500) was also employed in the secondary electron mode to obtain images of the LiOH corrosion layer grown on pressed polycrystalline LiH (by mechanically fracturing a sample of polycrystalline LiH salt in ambient air and examining the fractured surfaces). SEM was also used to examine the morphology of the thin corrosion layer after TPR heating to 550 K in vacuum.

Hydrogen outgassing from the $LiH/Li_2O/LiOH$ system was investigated mainly by TPR on 1 mm thick pressed polycrystalline LiH (100–200 μm grain size) with heating rates in the range of 0.0005–0.1 K/s. The TPR experiments involved two types of salt: fresh and baked. Fresh salt refers to salt samples with surfaces that have been polished with 1200 (P-4000) grit silicon carbide sand paper in an air-conditioned laboratory (400–600 Pa of H_2O partial pressure as measured by a Kahn dew-point hygrometer) to remove hydroxide/oxide surface layers. Immediately after the polishing step, fresh salt was attached to a molybdenum sample holder such that its top surface was exposed to room air for 21–30 min prior to the introduction into the TPR chamber. The room air exposure described above produced a LiOH corrosion layer with a mean thickness of 1.22 μm and an associated standard deviation of 0.11 μm as deduced from the mass spectrometer signals employed in the TPR experiments. Baked salt was fresh salt which had been heated to between 550 K and 580 K in a vacuum

to convert hydroxide into oxide (as verified by the mass spectrometer used in TPR experiments). After cooling down to room temperature under high vacuum, the baked samples were then reexposed to 3 Pa of H_2O pressure (30 ppm of H_2O) for 2.5 h. This H_2O reexposure resulted in the formation of a quantity of LiOH equivalent to a LiOH layer with a mean thickness of 0.28 μm and an associated standard deviation of 0.04 μm as deduced from the mass spectrometer signals employed in the TPR experiments. So, a significant reduction in the LiOH population is observed for baked salt (even after reexposure to 3 Pa of H_2O pressure for 2.5 h) in comparison with fresh salt. TPR was also performed on laboratory grade bulk LiOH powder (obtained from Fisher Chemicals) with grain sizes in the range of many tens of micrometers to a few hundreds of micrometers. Bulk LiOH powder samples were prepared by encapsulating about 45 mg of powder within a 1 cm^2 square platinum envelope. The envelopes were constructed from 0.025 mm thick platinum foil. The front face of each envelope was fully perforated to allow gases generated during TPR experiments to freely flow toward the mass spectrometer.

In a typical TPR experiment, the sample (attached to a molybdenum sample holder as described above) was transferred, through a differentially pumped load lock, into an ultrahigh vacuum (UHV) sample chamber with a base pressure of 10^{-6} Pa. Within the sample chamber, the sample holder sat on a rotatable XYZ manipulator. The sample temperature was measured via a type K thermocouple inserted between the sample's front surface (where all reactions under study happened) and one of the mounting clamps. Linear heating was achieved by resistive heating of a tungsten filament. The homemade tungsten resistive heating filament in our TPR setup had a cross section of ~250 μm and was shaped to form six concentric circular loops. All the loops were manually bent to lie on a plane located roughly 2 mm behind the molybdenum sample holder, to which a typical 1 mm thick by 1 cm diameter circular salt sample was attached. The innermost loop and outermost loop of the planar circular heating filament had diameters of about 2 mm and 13–14 mm, respectively. With the above described temperature measurement arrangement and heating setup, the variation in temperature obtained by placing the thermocouple at various places on the sample surface was less than 5 K (at 500 K using a heating

rate as high as 0.1 K/s). The heating rate was computer-controlled. The sample chamber was connected by a 6 mm diameter orifice to a separately pumped detector chamber equipped with a Balzers quadrupole mass spectrometer which was in line of sight of the sample. The base pressure in the detector chamber was usually less than 10^{-7} Pa. During the experiment, the sample was positioned ~2 mm from the orifice facing the detector chamber. This arrangement minimized contamination from gases originating from locations other than the portion of the sample in line with the 6 mm orifice.

In order to test the validity and accuracy of kinetic measurements and predictions based on the isoconversion analysis of TPR outgassing spectra, a set of long term (i.e., >180 days) isothermal outgassing experiments were undertaken. The isothermal outgassing experiments involved stored and annealed salt. Stored salt was maintained in an environment with ⩽10 ppm of H_2O, over an extended period of time, until insertion into previously baked and thoroughly outgassed steel containers equipped with Baratron capacitance gauges and valves for pump-down (by a turbo molecular pump). Annealed salt was stored salt which had been annealed in a dry environment (less than a few ppm of H_2O) at 503 K for 40 h, cooled down and then reexposed to 30 ppm of H_2O for 2–3 h. Diffuse reflectance infrared Fourier transform spectroscopy (DRIFT) indicated that the LiOH surface thickness was on the order of 0.26 μm for both stored and annealed salt. Similar to the case of fresh salt and baked salt described above, a significant reduction in the LiOH population is expected for annealed salt in comparison with stored salt. However, DRIFT measurements of LiOH thicknesses for stored and annealed salts were on the same order of magnitude. It is likely that DRIFT measurement of LiOH thickness on annealed salt is not as sensitive as mass spectrometer based measurement employed for baked salt. But due to the low equilibrium pressures of H_2O over the Li_2O/LiOH system [6], it is also possible that annealing salt to convert LiOH into Li_2O in a dry environment of a few ppm of H_2O is not as efficient as in an UHV environment (the case of baked salt). After pump down, the containers were placed within ovens set at different temperatures. Empty control vessels (no salt inside) served to establish a background outgassing level. At the end of the isothermal experiments, the gas content in each container was analyzed and found to be mostly H_2 (~99% H_2 and ~1% trace amounts of $N_2 + O_2 + Ar$). The H_2 outgassing properties of stored and annealed salt in isothermal experiments (performed at BWXT Y-12 facility in Oak Ridge, Tennessee) will be compared to those predicted from kinetic measurement of fresh and baked salt by TPR experiment (performed at Lawrence Livermore National laboratory in Livermore, California), respectively.

3. Analysis

The kinetics of the reactions were obtained by analyzing the TPR spectra of similarly prepared samples at different heating rates in accordance with the isoconversion method of thermal analysis as described below.

The rate equation for a solid-state reaction can be written as [7–10]:

$$\frac{d\alpha}{dt} = kf(\alpha) = \upsilon e^{-\frac{E}{RT}} f(\alpha), \tag{1}$$

where t is time; T is temperature in Kelvin; α is the reacted-fraction (0–1); υ is the pre-exponential factor which includes many constants describing the initial state of the sample such as three-dimensional shape factors of initial particles, molecular mass, density, stoichiometry, active surface factors, number of lattice imperfections, and so forth; E is the activation energy for the rate controlling process, R is the molar gas constant, and $f(\alpha)$ is an analytical function determined by the rate-limiting reaction mechanism. In this equation, $k = \upsilon e^{-\frac{E}{RT}}$ is the rate constant.

With a heating rate of $\beta = dT/dt$:

$$\frac{d\alpha}{dT} = \left[\frac{\upsilon}{\beta} f(\alpha)\right] e^{-\frac{E}{RT}}. \tag{2}$$

Taking the natural logarithm on both sides of Eq. (2) and integrating with respect to $d\alpha$ yields:

$$\int_0^\alpha \ln\left(\frac{d\alpha}{dT/\beta}\right) d\alpha = -\frac{E}{R} \int_0^\alpha \frac{d\alpha}{T} + \int_0^\alpha \ln\left(\upsilon f(\alpha)\right) d\alpha. \tag{3}$$

At any given α, the second term on the right-hand side of Eq. (3) is a constant, irrespective of the heating rate β. So, at a chosen value of α, a plot of $\int_0^\alpha \ln(\frac{d\alpha}{dT/\beta}) d\alpha$ vs. $\int_0^\alpha \frac{d\alpha}{T}$ for a set of different heating rates has a slope of $-E/R$. A plot of E vs. α is thus obtained by repeating the above procedure at other α values between 0 and 1 [11]. In practice, due to a poor signal-to-noise ratio near the beginning and

the end of most chemical reaction experiments, data outside an α range of 0.1–0.2 to 0.8–0.9 should be discarded.

With $g(\alpha) \equiv \int_0^\alpha \frac{d\alpha}{f(\alpha)}$ and for isothermal conditions:

$$g(\alpha) = \left[v e^{-\frac{E}{RT}} \right] \int dt = \left[v e^{-\frac{E}{RT}} \right] t. \qquad (4)$$

For non-isothermal conditions with a constant heating rate [12]:

$$g(\alpha) = \frac{v}{\beta} \int_0^T e^{-\frac{E}{RT}} dT \approx \frac{v}{\beta} \frac{RT^2}{E} e^{-\frac{E}{RT}}. \qquad (5)$$

The time, t_α, at which a given conversion α is reached at an arbitrary temperature T_0 can be approximated from non-isothermal experiments for many processes by equating the $g(\alpha)$ forms above for the isothermal and non-isothermal conditions [13,14]:

$$t_\alpha = \left[\beta e^{-\frac{E_\alpha}{RT_0}} \right]^{-1} \frac{RT_\alpha^2}{E_\alpha} e^{-\frac{E_\alpha}{RT_\alpha}}. \qquad (6)$$

Here, T_α is the temperature corresponding to a given conversion α at the heating rate of β. E_α is the value of the overall activation energy barrier at that level of conversion. For reactions in which E is not constant but increases with α, using Eq. (6) is equivalent to setting the kinetic parameters: E, v and $f(\alpha)$ fixed at $E = E_\alpha$, $v = v_\alpha$ and $f(\alpha) = f_\alpha$ from $\alpha = 0$ to that particular level of conversion α. Iterating Eq. (6) over every value of α yields a plot of t_α vs. α.

This isoconversion technique of analyzing TPR spectra does not assume any particular rate limiting model and so is suitable for the kinetic measurement and prediction of processes with competing reactions and/or an overall activation energy that varies with the conversion level.

4. Results and discussion

A typical AFM image of a polished salt surface is shown in the lower portion of Fig. 1. The units on the lateral scale and vertical scale are 2 μm and 1.5 μm per division, respectively. A line scan across the salt surface topography (upper portion of Fig. 1) reveals a surface roughness on the order of 0.5 μm. When LiOH films grew on these polished pressed polycrystalline LiH surfaces, they inherited a similar surface roughness and therefore had a three-dimensional (3D) topography.

Various morphologies of LiOH films grown on polycrystalline LiH surfaces are shown in Fig. 2.
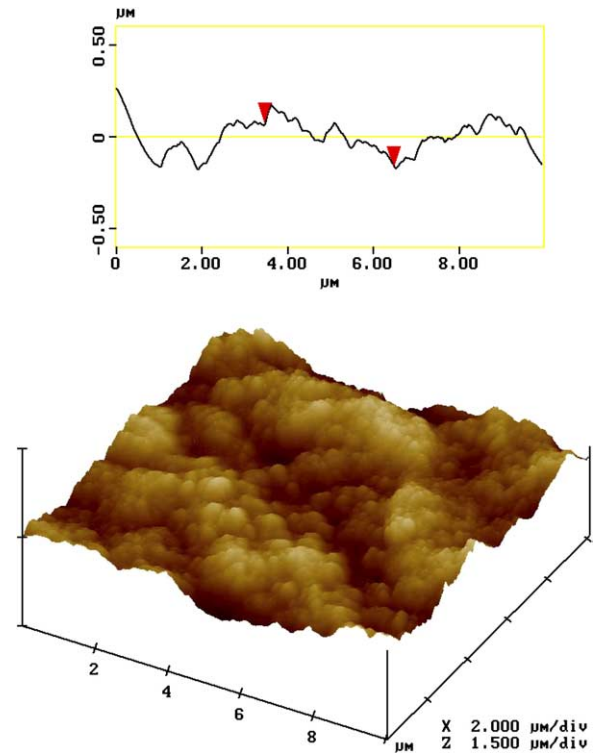

Fig. 1. AFM image of the surface roughness measured on pressed polycrystalline LiH. The top portion of this figure shows a line scan across the surface.

Depending on the LiH substrate facets, LiOH corrosion layers are composed of columnar structures with an average width on the order of a few hundred nanometers (a), nanometer-scale grains (b), wave like structures (c), and some complex nanometer-scale structures (d). Fig. 2(a)–(d) were obtained after the fractured surfaces of a mechanically fractured pressed polycrystalline LiH sample were exposed to roughly 15 min of room air with ~30% relative humidity (~951 Pa of H_2O partial pressure) at 296–300 K. The thickness of the LiOH films grown on these surfaces was estimated to be approximately 1.2 μm [15]. Fig. 2(e) and (f) show larger nanometer-scale grains observed on some facets of the fractured surfaces of another mechanically fractured polycrystalline LiH sample after exposure to room air for 40 min. The thickness of the LiOH films grown on these surfaces was estimated to be approximately 2 μm [15]. Due to large lattice and volume mismatches between LiH and LiOH [16], the formation of these nanometer-scale structures can be attributed to a stress relief mechanism during the growth of the LiOH layer.
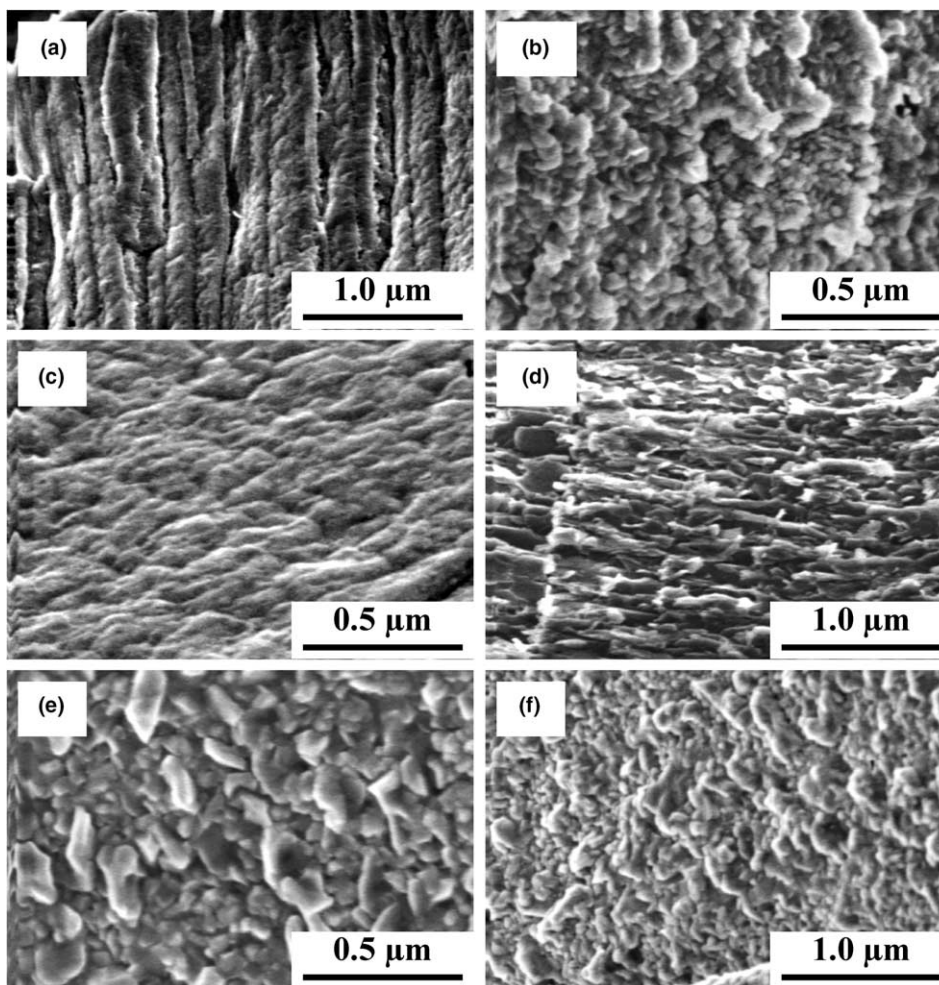
Fig. 2. SEM images of LiOH corrosion layer grown on different facets of pressed polycrystalline LiH after 15 min of air exposure at 30% relative humidity (a–d). Larger nanometer-scale grains observed by SEM on some facets of pressed polycrystalline LiH after exposure to room air for 40 min (e and f).

The integrity of the Li_2O layers grown on LiH salt as a result of heating to 550 K in vacuum is presented in Fig. 3. In general, the LiOH films under investigation were less than 1.5 μm thick and retained the majority of their integrity even after TPR heating. However, local spallation (the right portion of Fig. 3(a) and (d)), blistering with subsequent spallation (Fig. 3(b)), and blistering with cracks in the vicinity (Fig. 3(c)) were seen. This is in stark contrast to thick ($\gg 3$ μm) LiOH corrosion layers which tend to develop a large network of cracks to relieve stress-buildup during growth [4].

Fig. 4(a) shows the TPR spectrum of a fresh salt sample at a heating rate of 0.0015 K/s. The inset of Fig. 4(a) represents a blown-up portion of the same TPR spectrum in the lower temperature region. The

TPR spectrum for the decomposition of bulk LiOH powder at a heating rate of 0.002 K/s is shown in Fig. 4(b). In comparison with Fig. 4(b), the TPR spectrum in Fig. 4(a) may be considered to have two separate but competing reactions. One reaction involves H_2 formation via the reaction of LiOH with LiH forming Li_2O and the thereafter diffusion of OH^- from the $LiOH/Li_2O$ interface through the Li_2O buffer layer to react with the LiH substrate (lower temperature region in the TPR spectra where the H_2O signal is weak). This reaction will be discussed in detail later. The other reaction involves the decomposition of LiOH from the LiOH/vacuum surface inward, generating H_2O and forming Li_2O [4,5,7]. This component is weak in the lower temperature region but becomes more
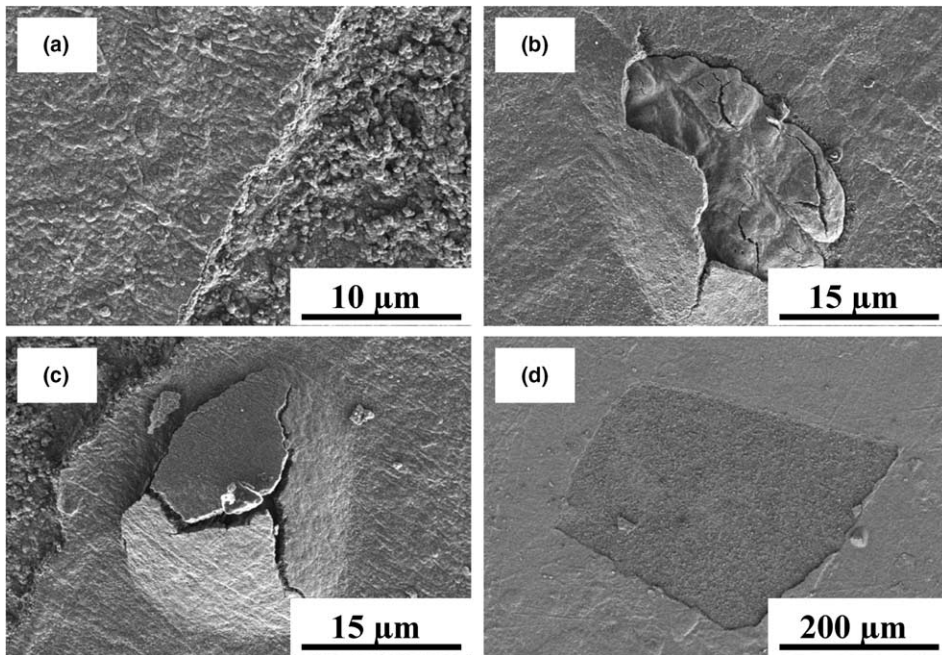
Fig. 3. Occasional spallations, blisters and cracks were observed in the morphology of the LiOH corrosion layer grown on polycrystalline LiH after TPR heating up to 550 K.
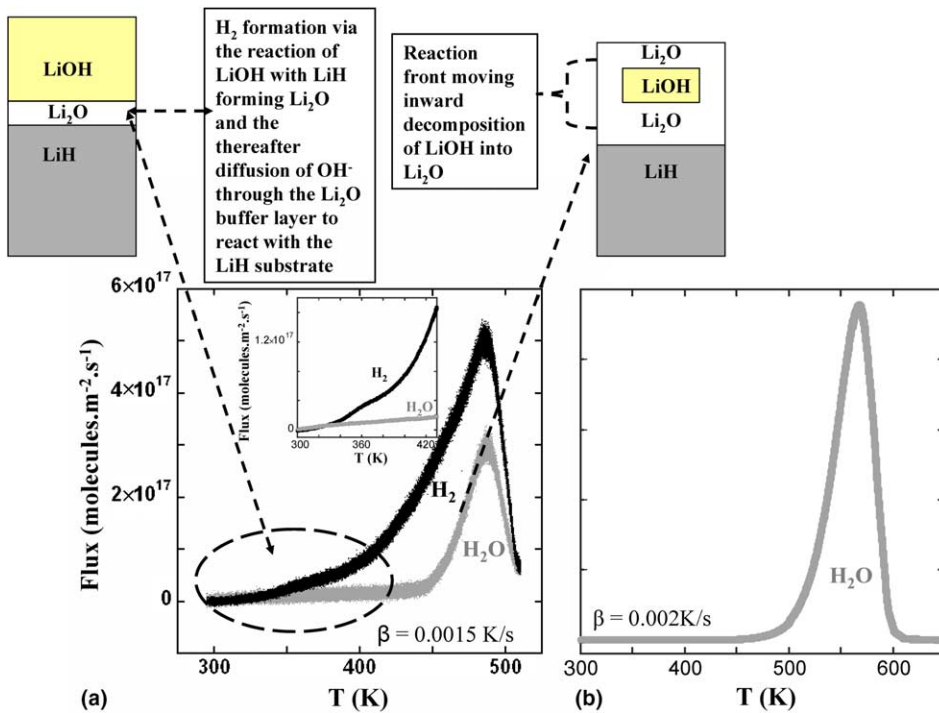

Fig. 4. (a) TPR spectrum of a fresh salt sample at a heating rate of 0.0015 K/s with accompanying cartoons illustrating the ongoing reactions (top) and a blown-up portion of the same spectrum in the lower temperature region (inset); (b) TPR spectrum of bulk LiOH powder decomposition at a heating rate of 0.002 K/s.

intense with increasing temperature and is dominant in the high temperature region (associated with a high mass 18 signal intensity seen in Fig. 4(a)). During TPR, some of the generated H_2O proceeded toward the LiH substrate to react and form H_2 while the rest moved toward the vacuum interface and was detected by the mass spectrometer. In a closed system containing LiH and LiOH, all H_2O generated from LiOH decomposition would rapidly react with LiH to form H_2 [3]. Thus, in the absence of any external H_2O source, LiOH is involved in all aspects of hydrogen outgassing from the LiH/Li$_2$O/ LiOH system. In earlier papers, some of the authors have reported the existence of some form of unstable surface/interface LiOH in addition to the more stable bulk LiOH [4,5]. In this report the existence of LiOH types, with varying propensities for decomposition, will be more rigorously analyzed.

LiOH reacts with LiH according to

$$LiOH(s) + LiH(s) \rightarrow Li_2O(s) + H_2(g) \qquad (7)$$
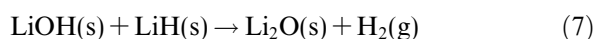
The heat of formation, ΔH, and Gibbs free energy, ΔG, for this reaction are -20 kJ/mol and -49 kJ/ mol at 273 K and reduce to -22 kJ/mol and -91 kJ/mol at 673 K, respectively [17].

Reaction (7) is so favorable (as evidenced by negative ΔH and ΔG values) that a Li$_2$O buffer is quickly formed in between LiH and LiOH, creating a LiOH/Li$_2$O/LiH interface [18]. Despite the initial formation of a buffer layer, further reaction is not inhibited, but simply gains a dependency on diffusion through the Li$_2$O. Initially, the stress/strain caused by lattice, volume and density mismatches at the LiOH/Li$_2$O/LiH double junction interface [16] weakens the bonds at that location. Since LiOH is the least thermally stable compound at that junction, the transport of OH$^-$ by diffusion from the LiOH/Li$_2$O interface through the Li$_2$O interlayer to react with LiH (as depicted in Fig. 5), is possible. At no point is water realized within this diffusive system. The diffusion of OH$^-$ species through the Li$_2$O layer is actually equivalent to an H$^+$ ion hopping between successive O$_2^-$ ions, with a transition state shown in (b). At the Li$_2$O/LiH interface the two oppositely charged hydrogen ions combine to generate hydrogen gas (c). An oxide ion shift occurs in order to minimize the energy of the subsequent crystalline void. The effective result is the diffusion of OH$^-$ through Li$_2$O. This solid-state diffusion reaction at the LiOH/Li$_2$O/LiH interface produces one mole of H_2 for the decomposition of every mole of LiOH at the LiOH/Li$_2$O interface.

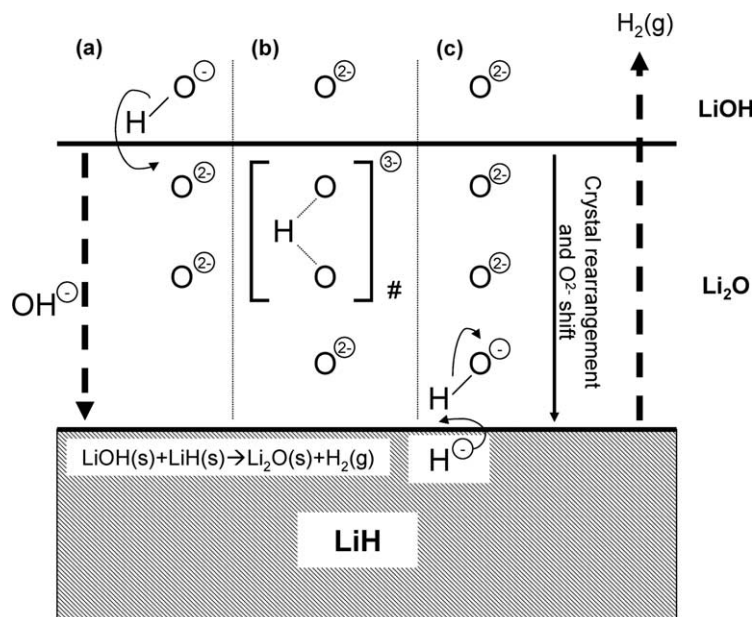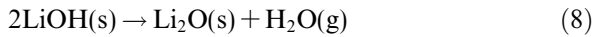Thermal decomposition of LiOH can be described as

Fig. 5. The diffusion of OH$^-$ through Li$_2$O. At no point is water realized within this diffusive system. (a) An H$^+$ ion can be seen to hop between successive O$_2$-ions with a transition state shown in (b). At the Li$_2$O/LiH interface the two oppositely charged hydrogen ions combine to generate hydrogen gas (c). An oxide ion shift occurs in order to minimize the energy of the subsequent crystalline void. The effective result is the diffusion of OH$^-$.

$$2LiOH(s) \rightarrow Li_2O(s) + H_2O(g) \qquad (8)$$

The heat of formation, ΔH, and Gibbs free energy, ΔG, for this reaction are 136 kJ/mol and 97 kJ/mol at 273 K and reduce to 127 kJ/mol and 43 kJ/mol at 673 K, respectively [17]. There are a number of experimental reports on the thermal decomposition of LiOH and the common consensus is that LiOH powder decomposes inwards from the LiOH/vacuum interface, while LiOH films grown on LiH decompose inwards from both the vacuum and substrate interfaces [3,5,19].

Out of all possible decomposition sites, interfacial LiOH at the LiOH/Li$_2$O/LiH double junction interface is the least stable as discussed above and shown in Fig. 4(a). Interface/surface states are also present at the LiOH/vacuum boundary (and possibly to some degree at LiOH grain surfaces). Surface LiOH states are expected to be thermally unstable in comparison with bulk LiOH. Due to defective and missing crystalline bonding at surface sites, lattice vibrations of surface material are at frequencies different to those of the bulk [20], a phenomenon seen in most solids. In addition, surface and interface species have different chemical reactivities and electronic properties to those of their bulk counterparts [20]. It should therefore be of no surprise to find that LiOH located at the LiOH/thin Li$_2$O/LiH double junction and LiOH at the LiOH/vacuum interface behave differently, in terms of thermal stability and reactivity, to LiOH in the bulk. During thermal decomposition of LiOH, as the Li$_2$O front moves far away from the LiH/vacuum interfaces, the activation energy for LiOH decomposition eventually increases to the level of bulk LiOH decomposition. Note that at temperatures below ∼450 K, the TPR mass 18 signal is non-zero and increases with heating temperature (inset of Fig. 4(a)), but is quite minimal compared to that of mass 2. This indicates that the H$_2$ production reaction at the LiOH/Li$_2$O/LiH interface and the H$_2$O production reaction due to thermal decomposition of LiOH grown on polycrystalline LiH are competing processes, with the former one having a smaller thermal barrier in the initial stage of outgassing when the Li$_2$O interlayer is thin.

In a closed system containing both LiH and LiOH, H$_2$O generated by thermal decomposition of LiOH rapidly reacts with LiH to form H$_2$ [3] according to

$$H_2O(g) + 2LiH(s) \rightarrow Li_2O(s) + 2H_2(g) \qquad (9)$$
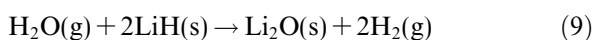
From the reaction sequence shown in (8) and (9), two LiOH decomposition events generate one intermediate H$_2$O molecule which, in turn, produces two H$_2$ molecules. Overall, there is one mole of H$_2$ formed for the decomposition of one mole of LiOH. In the TPR experiment on salt presented in Fig. 4(a), the H$_2$ signal (mass 2) originated from reaction (7) and the subsequent diffusion of OH$^-$ from the LiOH/Li$_2$O interface through the Li$_2$O buffer layer to react with the LiH substrate. In this same figure, the H$_2$O signal (mass 18) detected by the mass spectrometer originated from the LiOH decomposition reaction (8). In a closed environment containing both LiH and LiOH, each H$_2$O molecule generated from reaction (8) ultimately and quickly reacts with LiH to form two H$_2$ molecules according to reaction (9) [3]. Therefore, in vacuum device applications involving both LiH and LiOH, the total equivalent hydrogen outgassing flux ($\Gamma_{equiv.\,hydrogen}$, in units of molecule m^{-2} s^{-1}) can be approximated by doubling the mass 18 TPR flux ($\Gamma_{mass\,18}$) and adding the results to the mass 2 TPR flux ($\Gamma_{mass\,2}$):

$$\Gamma_{equiv.\,hydrogen} = 2\Gamma_{mass\,18} + \Gamma_{mass\,2}. \qquad (10)$$

Fig. 6 shows that the equivalent H$_2$ outgassing spectrum of the sample presented in Fig. 4(a) can be divided into two subcomponents, labeled D3 and R3. D3 and R3 simulated outgassing curves were obtained by regression fitting to Eq. (1), with $f(\alpha) = [1 - (1 - \alpha)^{1/3}]^2$ and $f(\alpha) = 1 - (1 - \alpha)^{1/3}$, respectively [10]. The D3 region represents the 3D solid-state diffusion controlled reaction at the
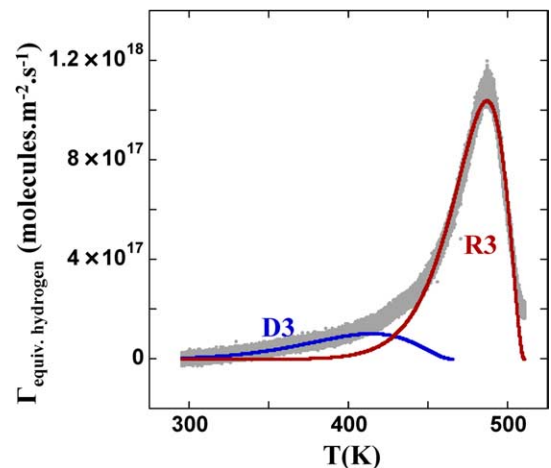

Fig. 6. The equivalent H$_2$ outgassing spectrum of the sample presented in Fig. 4(a) can be divided into two subcomponents labeled D3 and R3.

LiOH/Li$_2$O/LiH interface, with a constant activation energy of 69.9 kJ/mol. The solid state diffusion reaction contains a three-dimensional aspect, as opposed to 1D, to better describe effects introduced by the surface roughness of the polished salt samples, as shown in the AFM image of Fig. 1. The Li$_2$O thickness, x_{Li_2O}, formed at the LiOH/Li$_2$O/LiH interface can be approximated by

$$x_{Li_2O} = \frac{m_{Li_2O}}{\rho_{Li_2O}} \int \frac{\Gamma_{equiv.\ hydrogen}}{\beta} \, dT, \tag{11}$$

where m_{Li_2O} (4.98×10^{-26} kg molecule^{-1}) and ρ_{Li_2O} (2013 kg m^{-3}) are the mass of a Li$_2$O molecule and the density of bulk Li$_2$O, respectively. Eq. (11) suggests a Li$_2$O interlayer thickness on the order of 0.14 µm due to the solid-state diffusion reaction at the LiOH/Li$_2$O/LiH interface under the D3 regime. The R3 region represents mainly the thermal decomposition of LiOH with a progressive reaction front moving from the interface/surface inward [9] with a constant activation energy of 93.3 kJ/mol.

The two-part deconvolution of the total equivalent H$_2$ outgassing (Fig. 6) proves visually helpful in qualitatively identifying the different competing reactions, but assumes constant activation energies in the D3 and R3 regions. There is some degree of arbitrariness in the D3/R3 partitioning. If the assumption of 'constant activation energies' was not actualized in the real reactions or if the chosen models for the fit were not ideal, the accuracy of the kinetic prediction from this technique would greatly suffer. A model-independent kinetic analysis, which makes no assumption about constant activation energies for the competing reactions, is much more desirable. For this reason, from this point on, only kinetic measurements and predictions based upon the model-free isoconversion technique, which makes no assumption about the activation energy profile, will be presented.

Fig. 7 shows TPR spectra of total equivalent H$_2$ release rates in units of molecule m^{-2} s^{-1} from (a) fresh salt at $\beta = 0.0005$ K/s, (b) baked salt at $\beta = 0.005$ K/s, (c) fresh salt at $\beta = 0.025$ K/s, and (d) baked salt at $\beta = 0.025$ K/s. It is seen that the maximum outgassing peak shifted to a higher temperature as the heating rate was increased. The
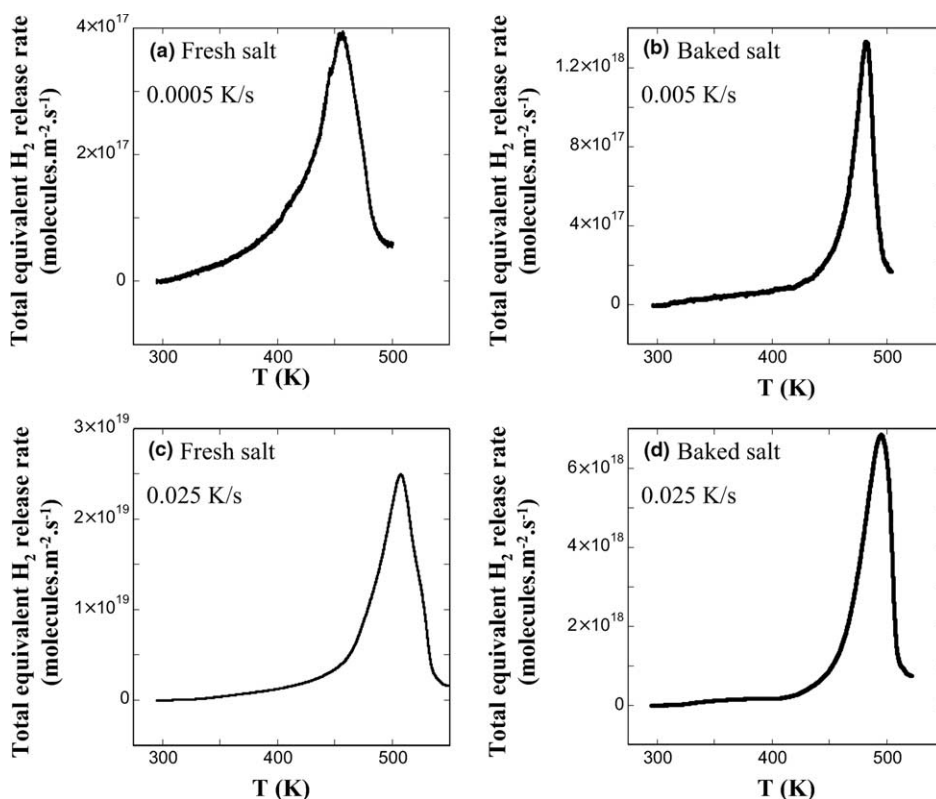

Fig. 7. TPR spectra of total equivalent H$_2$ release from (a) fresh salt at $\beta = 0.0005$ K/s, (b) baked salt at $\beta = 0.005$ K/s, (c) fresh salt at $\beta = 0.025$ K/s, and (d) baked salt at $\beta = 0.025$ K/s.

outgassing peak shifts presented in Fig. 7 are on the order of many tens of degrees in going from a very slow heating rate of 0.0005 K/s to a still reasonably slow heating rate of 0.025 K/s. The temperature shifts presented here are much larger than the few degrees differences expected across the salt sample's surface as mentioned in Section 2. So, the peak shifting to a higher temperature with increasing heating rate as presented in Fig. 7 is a clear indication of a thermal process with a positive activation energy barrier. Fig. 8 shows the plots of $\int_0^\alpha \ln(\frac{d\alpha}{dt})\,d\alpha$ vs. $\int_0^\alpha \frac{d\alpha}{T}$ for (a) fresh salt and (b) baked salt at α value of 0.3, 0.5, and 0.7. The plots in Fig. 8 were obtained by taking TPR spectra at different heating rates. Linear regression through the $\int_0^\alpha \ln(\frac{d\alpha}{dt})\,d\alpha$ vs. $\int_0^\alpha \frac{d\alpha}{T}$ data at different values of α from 0.15 to 0.9 give a plot of E vs. α for the hydrogen outgassing process from each type of salt. Plots of E vs. α for fresh salt (middle curve) and baked salt (lower curve) are presented in Fig. 9, together with the activation energy plot for LiOH decomposition obtained from bulk LiOH powder TPR experiments (top curve). The outgassing process from thin LiOH films grown on LiH is seen, here, as a complicated process involving competing reactions with an overall activation energy barrier that increases with reacted-fraction, α. The activation energy barrier for hydrogen outgassing from baked salt with an equivalent LiOH layer thickness of $\sim$0.28 μm is observed to be much lower, and have a different shape, to that of fresh salt with a mean LiOH layer thickness of 1.22 μm. This can be understood by the following. Vacuum baking of the LiH/LiOH system at high temperature converts LiOH into Li_2O with the formation of local spallations and cracks within the Li_2O region to relieve stress.
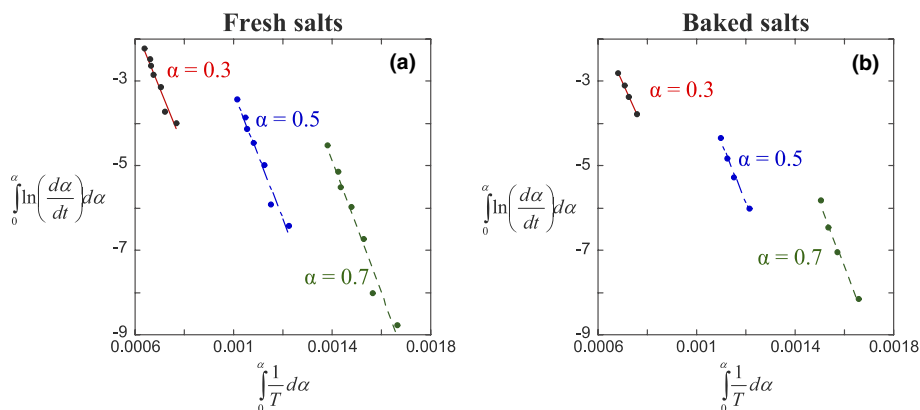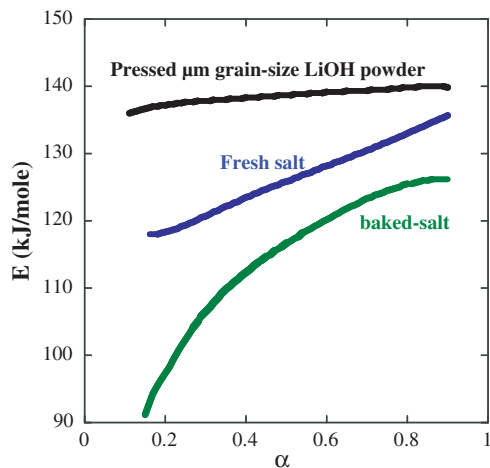

Fig. 9. Activation energy vs. α plots for outgassing from LiOH powder and each type of salt studied.

Upon subsequent low H_2O exposure for 2.5 h, only a small population of Li_2O (more abundantly near surfaces and defect locations) is converted back to LiOH. As mentioned earlier in this report, due to defective and missing crystalline bonding at surface sites, surface/interface LiOH is expected to be thermally unstable in comparison with bulk LiOH. And since the ratio of interface/surface LiOH to bulk LiOH was much higher in systems baked and reexposed to low H_2O pressure, the activation energy barrier for the decomposition of LiOH formed on baked salt was expected and experimentally verified to be lower than that for fresh salt. Similarly, the activation energy barrier for hydrogen outgassing from fresh salt is seen to progressively increase with α and is expected to approach that of bulk LiOH powder decomposition for thicker, multi-micron,

Fig. 8. The plots of $\int_0^\alpha \ln(\frac{d\alpha}{dt})\,d\alpha$ vs. $\int_0^\alpha \frac{d\alpha}{T}$ for (a) fresh salt and (b) baked salt at α value of 0.3, 0.5, and 0.7.
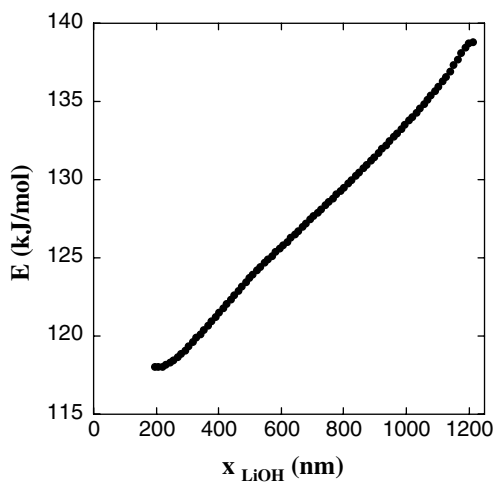
Fig. 10. A plot of the activation energy barrier for outgassing vs. the equivalent LiOH decomposition thickness for fresh salt.

LiOH corrosion layers. This is easily seen if the activation energy barrier for outgassing is plotted vs. the equivalent LiOH decomposition thickness for fresh salt (Fig. 10), where the LiOH decomposition thickness, x_{LiOH}, is derived according to

$$x_{LiOH} = \frac{m_{LiOH}}{\rho_{LiOH}} \int \frac{\Gamma_{equiv.\,hydrogen}}{\beta} \, dT. \qquad (12)$$

In Eq. (12), m_{LiOH} (3.99×10^{-26} kg molecule^{-1}) and ρ_{LiOH} (1460 kg m^{-3}) are the mass of a LiOH molecule and the density of bulk LiOH, respectively. During moisture bombardment, most of the LiOH formed early in the process is surface/interface LiOH. However, there is a limit to the number of sites available to form surface/interface LiOH. Once these sites are used up, the remaining LiOH creation is almost exclusively bulk. As a result, one expects an inverse relationship between the activation energy barrier for hydrogen outgassing in the LiH/Li$_2$O/LiOH system and the LiOH corrosion layer thickness. Indeed, this is the reason why the H$_2$O peak from bulk LiOH powder decomposition TPR spectrum in Fig. 4(b) is shifted by ~80 K to a higher temperature in comparison with the H$_2$O peak from the fresh salt TPR spectrum in Fig. 4(a), given their very small difference in heating rate.

A comparison between experimental isothermal hydrogen outgassing from stored salt, with a total geometrical surface area of 0.0190 m^2, and an outgassing prediction based on the model-free kinetic analysis for fresh salt, with a similar surface area, at 343 K is presented in Fig. 11(a). Fig. 11(b)–(d) show comparisons between experimental isothermal hydrogen outgassing from annealed salt, with a total

geometrical surface area of 0.0205 m^2, and outgassing predictions based on the model-free kinetic analysis for baked salt at 348.7 K, 330.1 K and 315.5 K, respectively. The heavy lines indicate experimental isothermal hydrogen outgassing data while the lighter bands are predicted from the isoconversion kinetic analysis of TPR spectra. Despite noticeable scatters in the experimental isothermal outgassing curves, it is recognized that experimental and predicted curves correlate well. Inconsistencies, in particular between (c) and (d) where increased outgassing is seen at the lower temperature, are due to unavoidable sample to sample variations, assembly conditions and instrument response, but are to be expected over long term trials such as these. Given these unavoidable differences in preparation conditions and variations in LiH sample treatment between TPR (Lawrence Livermore National Laboratory, California) and isothermal (BWXT Y-12 Laboratory, Tennessee) experiments, the majority of the isothermal data falls within the kinetic prediction bounds and more importantly the curve shapes are well represented, adding additional credence to the reacted-fraction dependent activation energies. Using the methodology presented here, and with the help of Eq. (6), time dependent kinetic predictions for hydrogen release from the LiH/LiOH system can be made at any temperature and as a function of sample pre-treatment.

5. Conclusions

In summary, the technique of temperature programmed reaction/decomposition was applied in conjuction with the isoconversion method of thermal analysis to make kinetic predictions for the hydrogen outgassing profile of the polycrystalline LiOH/Li$_2$O/LiH system. The outgassing predictions based on the measured kinetics agree well with experimental isothermal outgassing data. In the course of this work, it is found that LiOH, in particular LiOH at the LiOH/thin Li$_2$O/LiH and LiOH near the LiOH/vacuum interface, is involved in all aspects of hydrogen outgassing. Mechanisms for such a process have been proposed. Experimental results presented in this report also reveal that the initial activation energy for outgassing from the thin LiOH film grown on LiH is significantly lower than that for bulk LiOH decomposition, but increases as the reaction proceeds, approaching the bulk LiOH value in multi-micrometer thick films. The methodology presented in this report can be used to generate isothermal hydrogen outgassing predictions for
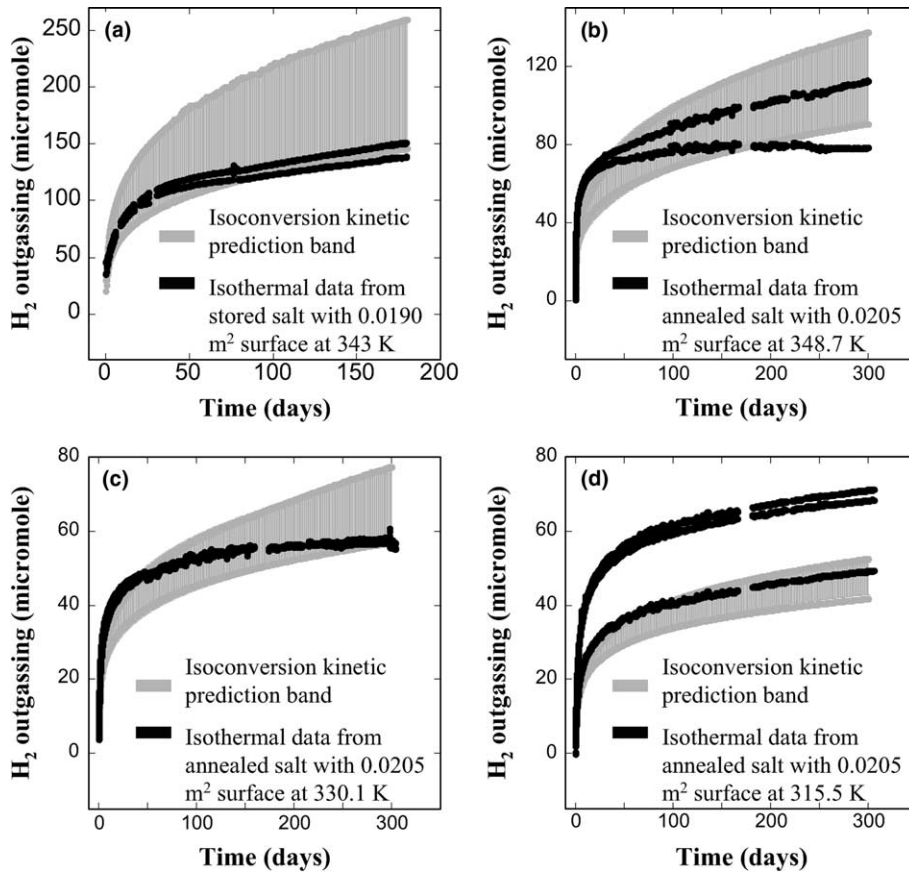
Fig. 11. Comparison between experimental isothermal hydrogen outgassing and isoconversion kinetic prediction for stored/fresh salt at 343 K (a) and annealed/baked salt at 348.7 K (b), 330.1 K (c) and 315.5 K (d).

LiH/LiOH under a variety of initial environmental conditions.

Acknowledgements

Appendix A

For thin LiOH films grown on LiH in high moisture conditions (H_2O partial pressure on the order of a few hundred Pascal or more), the average film growth thickness, x, as a function of time, t can be approximated by Fick's law:

$$J = -D\frac{\Delta C}{\Delta x} \approx -D\frac{C_{surface}}{x}. \qquad (I)$$

Here J is the flux of H_2O at the LiH surface in units of molecule $m^{-2}\,s^{-1}$, D is the diffusion coefficient of H_2O in the LiOH layer in units of $m^2\,s^{-1}$ and $C_{surface}$ is the H_2O concentration at the LiOH/vacuum interface in units of molecule m^{-3}.

But

$$\frac{dx}{dt} = -\frac{J}{C_{in\,solid}}. \qquad (II)$$

In Eq. (II), $C_{in\,solid}$ is the concentration of OH^- in the LiOH corrosion layer in units of molecule m^{-3}.

From (I) and (II):

$$\frac{dx}{dt} = D\frac{C_{surface}}{C_{in\,solid}}\frac{1}{x} \qquad (III)$$

or

$$x^2 = 2\frac{C_{surface}}{C_{in\,solid}}Dt + A. \qquad (IV)$$

In Eq. (IV), A is some initial value of x^2 at $t = 0$ which can be set to 0 in the present case. Taking the square root on both sides of Eq. (IV) yields:

$$x = \sqrt{2\left[D\left(\frac{C_{\text{surface}}}{C_{\text{in solid}}}\right)\right]t}. \tag{V}$$

Here are some approximated values:

$$C_{\text{in solid}} = \frac{\rho_{\text{LiOH}}}{m_{\text{LiOH}}} = \frac{1450 \ (\text{kg m}^{-3})}{4 \times 10^{-26} \ (\text{kg molecule}^{-1})}$$
$$= 3.63 \times 10^{28} \ (\text{molecule m}^{-3})$$

$D\left(\frac{C_{\text{surface}}}{C_{\text{in solid}}}\right)$ is on the order of $5 \times 10^{-16} \text{ m}^2 \text{ s}^{-1}$ for moisture exposure at room temperature with a 18–30% relative humidity.

References

[1] W.D. Machin, F.C. Tompkins, Trans. Faraday Soc. 62 (1966) 2205.

[2] M. Balooch, L.N. Dinh, D.F. Calef, J. Nucl. Mater. 303 (2002) 200.

[3] S.M. Myers, J. Appl. Phys. 45 (1974) 4320.

[4] L.N. Dinh, C.M. Cecala, J.H. Leckey, M. Balooch, J. Nucl. Mater. 295 (2001) 193.

[5] L.N. Dinh, W. McLean II, M.A. Schildbach, J.D. LeMay, W.J. Siekhaus, M. Balooch, J. Nucl. Mater. 317 (2003) 175.

[6] H. Takeshita, H. Watanabe, J. Nucl. Mater. 207 (1993) 92.

[7] C.H. Bamford, C.H.F. Tipper, Comprehensive Chemical Kinetics: Reaction in the Solid State, vol. 22, Elsevier, Amsterdam, 1980, p. 41.

[8] K. Heide, W. Holand, H. Golker, K. Seyfarth, B. Muller, R. Sauer, Thermochim. Acta 13 (1975) 365.

[9] A.M. Gadalla, Thermochim. Acta 95 (1985) 179.

[10] A.K. Galwey, M.E. Brown, Thermal Decomposition of Ionic Solids, Elsevier, New York, 1999.

[11] C.-R. Li, T.B. Tang, J. Mater. Sci. 34 (1999) 3467.

[12] K.H. Van Heek, H. Juntgen, Ber. Bunsenges. Phys. Chem. 72 (1968) 1223.

[13] S. Vyazovkin, C.A. Wight, Annu. Rev. Phys. Chem. 48 (1997) 125.

[14] S.V. Vyazovkin, A.I. Lesnikovich, Russ. J. Phys. Chem. 62 (1988) 1535.

[15] See Appendix A.

[16] LiH has a cubic structure with a lattice parameter of $a = 4.083$ Å and a unit cell volume of 68.1 Å^3. LiOH has a tetragonal structure with lattice parameters of $a = 3.553$ Å, $c = 4.348$ Å and a unit cell volume of 54.9 Å^3. Li$_2$O has a cubic lattice structure with a lattice parameter of $a = 4.611$ Å and a unit cell volume of 98.1 Å^3.

[17] HSC Chemistry for Windows, Outokumpu Research Oy, Finland.

[18] J.F. McLaughlin, S.S. Cristy, Composition of Corrosion Films on Lithium Hydride Surfaces After Exposure to Air, report # Y-1929, Oak Ridge Y-12 Plant, 1974.

[19] J.M. McIntyre, H.M. Smith, American Chemical Society Paper Abstract for the S.E. and S.W. Regional Meeting, 2–4 December 1970, p. 174.

[20] H. Lüth, Solid Surfaces, Interfaces and Thin Films, Springer, Berlin, 2001.